



Ordered mesoporous Ni/La₂O₃ catalysts with interfacial synergism towards CO₂ activation in dry reforming of methane

Kang Li^{a,b}, Xin Chang^{a,b}, Chunlei Pei^{a,b}, Xinyu Li^{a,b}, Sai Chen^{a,b}, Xianhua Zhang^{a,b},
Suttichai Assabumrungrat^c, Zhi-Jian Zhao^{a,b}, Liang Zeng^{a,b}, Jinlong Gong^{a,b,*}

^a Key Laboratory for Green Chemical Technology of Ministry of Education, School of Chemical Engineering and Technology, Tianjin University, Tianjin 300072, China

^b Collaborative Innovation Center of Chemical Science and Engineering, Tianjin 300072, China

^c Department of Chemical Engineering, Faculty of Engineering, Chulalongkorn University, Bangkok 10330, Thailand

ARTICLE INFO

Keywords:

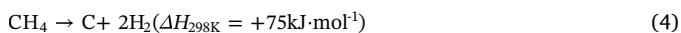
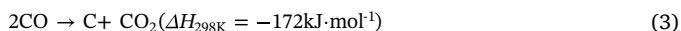
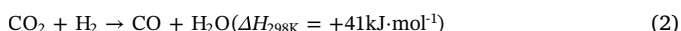
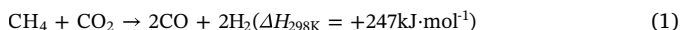
Mesoporous La₂O₃
Bidentate carbonate
Monodentate carbonate
Metal support interface
CO₂ activation

ABSTRACT

This paper describes the synthesis of ordered mesoporous Ni/La₂O₃ catalysts (denoted as Ni/La₂O₃-m) for dry reforming of methane and investigates the synergistic effect of Ni/La₂O₃ interfaces on the activation of CO₂. The resultant nanostructured La₂O₃ possessed high specific surface area of 211.5 m²/g, and Ni/La₂O₃-m catalysts maintained the initial morphology upon thermal treatment. The mesostructure was beneficial to obtain and maintain Ni nanoparticles with sizes between 4–6 nm. Ni/La₂O₃-m catalysts exhibited superior activity and stability in dry reforming of methane, showing excellent performance in activating both CH₄ and CO₂ due to more catalytically active Ni sites and increased interfaces. *In situ* DRIFTS indicated that bidentate carbonate participates in coke elimination. Combined with CO₂-TPD and density functional theory (DFT) calculations, we found that Ni/La₂O₃-m catalyst has stronger capability to promote the formation of bidentate carbonate due to the increased interfaces by enhancing Ni dispersion, which leads to better stability by suppressing the coke deposition.

1. Introduction

Dry reforming of methane (DRM, Reaction 1) has received increasing attention as a promising approach for syngas production from natural gas with high concentration of CO₂ [1–3]. The resulting syngas is suitable for Fischer-Tropsch (FT) synthesis of long chain hydrocarbons [4] and oxygenated derivatives [5]. According to the thermodynamic analysis, DRM requires elevated temperatures (above 600 °C) to attain high equilibrium conversions [6,7]. At such high temperatures, the major practical issue preventing commercialization of DRM is that the catalysts experience deactivation or destruction due to severe carbon deposition [8].



Nickel-based catalysts have the advantages of high activity and wide availability [2,8,9]. However, severe carbon deposition and metal

sintering limit their applications in DRM. A recent review by our group summarized encapsulated structures are capable to inhibit metal sintering [10]. The key to inhibiting carbon deposition is that the carbon species produced from activation of CH₄ could be removed by CO₂-derived species in time [11,12]. Comas-Vives et al. found that oxygen species derived from CO₂ activation can react with C-H* to form CHO*, thereby avoiding deep dehydrogenation to form coke [13]. Therefore, promoting CO₂ activation is crucial to the stability of DRM reaction. Several methods have been investigated to promote CO₂ activation, including bimetallic catalysts and promotion additives [14–19]. Galvita et al. studied that the crystal structure evolution of bimetallic NiFe catalysts by time-resolved *in-situ* XRD. They found that Fe was oxidized to FeO_x by CO₂ and surface carbon was removed by lattice oxygen from FeO_x [20]. Liu et al. investigated the Ga₂O₃ modified Ni/SiO₂ catalyst, and concluded that Ga₂O₃ can promote CO₂ activation to inhibit carbon deposition [16]. In addition, alkaline supports can be used [11,21] to help activate CO₂ and provide oxygen species to eliminate carbon deposits. Lercher et al. demonstrated that Pt/ZrO₂ catalyst has better coke resistance than Pt/Al₂O₃ because of the capability of ZrO₂ in CO₂ activation [22]. Among many alkaline supports, La₂O₃ is one of the most studied supports because of its excellent capability to activate CO₂ [23–28].

* Corresponding author.

E-mail address: jlgong@tju.edu.cn (J. Gong).

<https://doi.org/10.1016/j.apcatb.2019.118092>

Received 31 May 2019; Received in revised form 7 August 2019; Accepted 13 August 2019

Available online 14 August 2019

0926-3373/ © 2019 Elsevier B.V. All rights reserved.

Ni/La₂O₃ catalyst generally follows a dual site reaction mechanism: methane activation generates hydrogen and coke precursors on the surface of Ni, while CO₂ activation occurs on the La₂O₃ support [23,28]. Although La₂O₃ has good performance for inhibiting carbon deposition, the low surface area strongly restricts its applications [26,29,30]. To solve this problem, La₂O₃ was dispersed on supports with large specific surface area [29,31] and mineral-type precursors were used [32,33]. In addition, the selection of metals and supports can affect the performance of Ni/La₂O₃ catalyst, especially the activation of CO₂. Müller et al. introduced Co on the Ni/La₂O₃ catalyst to promote the formation La₂O₂CO₃ which helps inhibit carbon deposition [34]. Irusta et al. reported that noble metals (Rh, Pt) can affect CO₂ activation on La₂O₃ [35,36]. Our recent research found that different carbonate species have different reactivity for DRM, and the addition of Ce can promote CO₂ activation to form active intermediate [37]. However, so far there remains many issues including why metals can affect the activation of carbon dioxide and why different CO₂-derived species have different reactivity. The interface between metal and support is typically considered as the active site for reactions taking place [23,25,38,39], which makes it necessary to study the behavior of CO₂ activation at Ni/La₂O₃ interface. In addition, reaction between CO₂-derived species and coke is a rate-determining step for the coke elimination process. However, the detailed mechanistic understanding of such process is still under debate [40].

This work is to introduce a new approach for synthesizing Ni based DRM catalyst supported on ordered mesoporous La₂O₃ and to illustrate the role of Ni/La₂O₃ interface in CO₂ activation. *In situ* DRIFTS and TPSR technology were performed to study the role of various intermediates formed in DRM reaction. CO₂-TPD was used to quantitatively characterize the number of various basic sites. The physical-chemical properties of the catalysts were investigated by N₂-physisorption, XRD, H₂-TPR and TEM. All the above-mentioned experimental studies together with DFT calculations can lead to a deeper understanding of the DRM reaction mechanism over Ni/La₂O₃ catalyst.

2. Experimental and computational methods

2.1. Preparation of catalysts

Mesoporous La₂O₃ was synthesized according to the method reported by Schüth et al [41]. First, silanol group rich SBA-15 was hydrothermally prepared. Under stirring condition, 4.0 g P123 was dissolved in 20 mL of 37 wt.% HCl and 130 mL of H₂O at 38 °C, after which 8.0 g of tetraethylorthosilicate (TEOS) was added. The mixture was stirred at 38 °C for 24 h and then hydrothermally treated at 110 °C for another 24 h. Afterwards, the precipitate obtained by centrifuging the mixture was washed and dried at 80 °C. 2.0 g of the obtained white powder was dissolved in 30 mL of 65 wt.% HNO₃ and 15 mL of 30 wt.% H₂O₂ at 80 °C for removing P123 template. The suspension was then refluxed for 3 h. The SBA-15 template was obtained by centrifugation, washed with water and anhydrous ethanol, and then dried at 50 °C. Next, La₂O₃-m was synthesized by the prepared SBA-15 template. Typically, 1.3 g La(NO₃)₃·6H₂O was dissolved in 700 µL of 1.07 mol/L HNO₃ to obtain an aqueous solution. The solution was then impregnated onto 0.5 g SBA-15 template. Then the mixture was sealed and aged at 50 °C for one day, aged at 90 °C for another two days, and calcined at 650 °C for 5 h with a heating rate of 1 °C/min. Finally, the SBA-15 template was removed by 2 mol/L NaOH solution at 70 °C for 24 h.

Ni/La₂O₃-m catalyst was prepared *via* incipient wetness impregnation. The supports were impregnated with the Ni(NO₃)₂·6H₂O solution to yield catalysts with 5 wt.% Ni content. Then, the sample was dried at 120 °C for 12 h and calcined at 650 °C for 4 h. The catalyst was made into powder with grain sizes between 20–40 mesh.

For comparison, a reference Ni/La₂O₃ catalyst was prepared. The La₂O₃ support was prepared by calcinating La(NO₃)₃·6H₂O under

nitrogen atmosphere at 650 °C for 8 h. Then, Ni/La₂O₃ catalyst was obtained by the above method. The prepared samples were named as La₂O₃-n and 5Ni/La₂O₃-n, where n represents the preparation of La₂O₃ by calcining nitrate precursor. A reference 5Ni/Al₂O₃ catalyst was also prepared by the same method and calcined at 600 °C for 4 h to obtain Ni particle size similar to 5Ni/La₂O₃-m catalyst.

2.2. Catalytic activity tests

The activity test was conducted under ambient pressure. 25 mg catalyst diluted with 1 mL of quartz particles (20–40 mesh) was loaded into a fixed-bed tubular quartz microreactor. The catalyst was reduced with a H₂/N₂ mixture (10 vol.%, 100 mL/min) at 650 °C for 1 h and then purged with a N₂ flow (90 mL/min) for 30 min to remove hydrogen in the reactor. Next, the reactant gas mixture with a CH₄:CO₂:N₂ volume ratio of 15:15:70 was introduced for activity tests. The total flow rate was 100 mL/min. The conditions were chosen to ensure that the reaction was not operating near equilibrium conditions. A K-type thermocouple was inserted in the tubular quartz in order to measure the catalyst temperature during experiments. The gas species were analyzed online by a gas chromatograph.

The conversion of the CH₄/CO₂ and the selectivity of the products were calculated as follows:

$$X_{\text{CH}_4} = \frac{F_{\text{CH}_4,\text{in}} - F_{\text{CH}_4,\text{out}}}{F_{\text{CH}_4,\text{in}}} \times 100\%$$

$$X_{\text{CO}_2} = \frac{F_{\text{CO}_2,\text{in}} - F_{\text{CO}_2,\text{out}}}{F_{\text{CO}_2,\text{in}}} \times 100\%$$

$$S_{\text{H}_2} = \frac{F_{\text{H}_2}}{2 \times (F_{\text{CH}_4,\text{in}} - F_{\text{CH}_4,\text{out}})} \times 100\%$$

$$S_{\text{CO}} = \frac{F_{\text{CO}}}{(F_{\text{CH}_4,\text{in}} + F_{\text{CO}_2,\text{in}}) - (F_{\text{CH}_4,\text{out}} + F_{\text{CO}_2,\text{out}})} \times 100\%$$

$$Y_i = X_j \times S_i \times 100\% \quad (i = \text{H}_2 \text{ or CO}, j = \text{CH}_4 \text{ or CO}_2)$$

$$\frac{\text{H}_2}{\text{CO}} = \frac{F_{\text{H}_2}}{F_{\text{CO}}}$$

2.3. Characterization

N₂ physisorption was conducted to measure the specific surface areas of samples with a Micromeritics Tristar 3000 analyzer at −196 °C. The sample (100 mg) was degassed at 90 °C for 1 h and 300 °C for 3 h in flowing nitrogen atmosphere before the measurement. The specific surface areas were calculated using the BET method. The average pore diameters and pore volumes were obtained using the BJH method.

Elemental contents of the samples were examined by ICP-OES (VISTA-MPX, Varian). Prior to experiment, the sample was added to hydrofluoric acid solution to dissolve the residual SiO₂ template, then nitric acid was added to dissolve La₂O₃ and Ni. Finally, the concentrations of measured elements were adjusted based on standard solutions.

XRD analysis of samples was conducted by a Rigaku D/max-2500 diffractometer with Cu Kα X-ray source (λ = 1.54056 Å). The diffraction was performed over 2θ range of 0.5–5 ° (low-angle) and 20–80 ° (wide-angle). The mean nickel particle sizes were estimated *via* Ni (111) facet diffraction peaks in the samples using the Scherrer equation.

H₂-TPR was conducted on Micromeritics AutoChem II 2920, equipped with a TCD and MS instrument. Before the experiment, the sample (100 mg) was degassed to remove adsorbed impurities at 300 °C for 1 h. A H₂/Ar flow (10 vol.%, 30 mL/min) was introduced after cooling the temperature to 80 °C, and the temperature was raised to

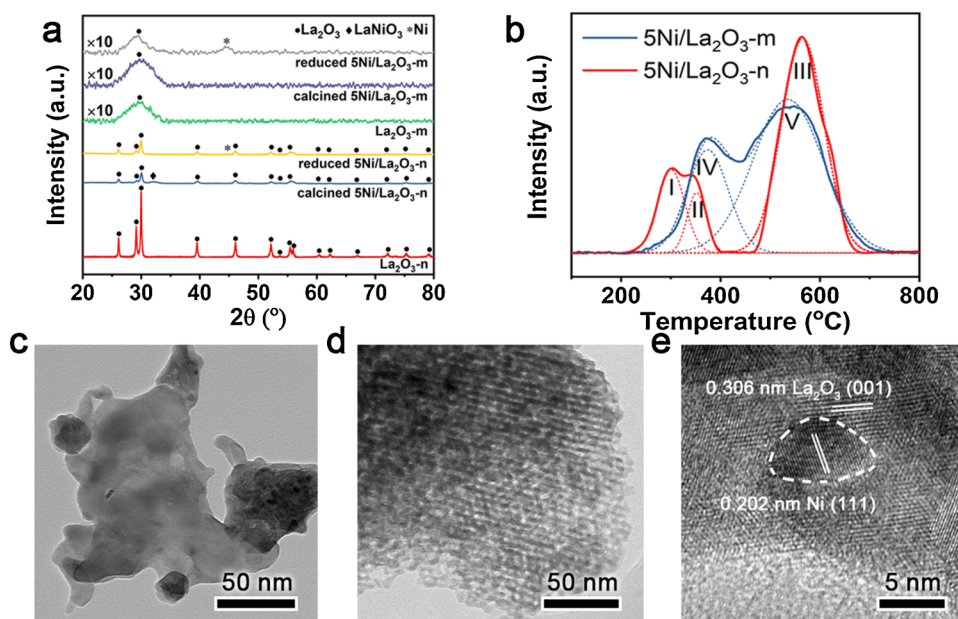


Fig. 1. Characterization of calcined and reduced catalysts. **a** XRD patterns of the samples. **b** H_2 -TPR results of the catalysts. **c** TEM image of reduced 5Ni/La₂O₃-n catalyst. **d** TEM image of reduced 5Ni/La₂O₃-m catalyst. **e** TEM image of Ni and La₂O₃ interface in 5Ni/La₂O₃-n catalyst.

900 °C with a heating rate of 10 °C/min. The TCD signals together with the MS signals were recorded simultaneously. Water formed during the process was removed with a cooling trap.

Ni metal dispersion and active surface area were measured using the same chemisorption analyzer. Before the experiment, the sample (100 mg) was reduced with a H_2/Ar flow (10 vol.%, 30 mL/min) at 650 °C for 1 h, then purged with an Ar flow (30 mL/min) and the temperature was cooled down to 50 °C. Thereafter, several H_2 pulses were injected for chemisorption until the elution peak of the continuous pulse remained constant. Ni metal dispersion and active surface area were obtained from the amount of chemisorbed hydrogen based on the surface area of each Ni atom ($6.5 \times 10^{-20} \text{ m}^2$) and $\text{H}_{\text{adsorbed}}/\text{Ni}_{\text{surface}}$ stoichiometric ratio (1) [42].

CO_2 -TPD was performed to quantitatively measure the number of various basic sites on the sample. The sample (100 mg) was reduced with a H_2/Ar flow (10 vol.%, 50 mL/min) at 650 °C for 1 h. The sample was then cooled to 60 °C and subsequently exposed to a CO_2 flow (50 mL/min) until saturated coverage was reached. The temperature was raised to 120 °C to get rid of the weakly adsorbed carbon dioxide by He flushing. The temperature was then raised to 800 °C with a linear rate of 3 °C/min, and the TCD signals together with the MS signals were recorded simultaneously.

CH_4 -TPSR, CO_2 -TPSR and CO_2/CH_4 -TPSR were performed to study the activation and reaction mechanism of CH_4 and CO_2 molecules on the catalysts. Before the experiment, the sample (100 mg) was reduced with a H_2/Ar flow (10 vol.%, 30 mL/min) at 650 °C for 1 h. Regarding CH_4 -TPSR, a CH_4 flow (30 mL/min) was introduced to react with reduced sample (100 mg) and the temperature was raised from 60 to 700 °C with a heating rate of 10 °C/min. In the case of CO_2 -TPSR, the reduced sample (100 mg) was exposed to a CH_4 flow (30 mL/min) at 650 °C for 10 min. The sample was then cooled to 60 °C. Then a CO_2 flow (30 mL/min) was introduced to react with the sample and the temperature was raised from 60 to 700 °C with a heating rate of 10 °C/min. As for CO_2/CH_4 -TPSR, the reduced sample (100 mg) was exposed to a CO_2 flow (50 mL/min) at 60 °C until saturated coverage was reached. Then a CH_4 flow (30 mL/min) was introduced to react with the sample and the temperature was raised from 60 to 700 °C with a heating rate of 10 °C/min. The MS signals were recorded during the process.

The morphology of the samples was analyzed using a FEI Tecnai G2 F20 transmission electron microscope under a working voltage of

100 kV.

Thermogravimetric analysis was performed with a TGA instrument (STA449F3, NETZSCH Corporation). In the experiment, the air flow rate was 80 mL/min and the temperature was raised from 35 to 800 °C with a linear rate of 10 °C/min.

In situ DRIFTS was carried out on a ThermoFisher Nicolet IS50 spectrometer equipped with a Harrick Scientific diffuse reflection accessory and a mercury-cadmium-telluride (MCT) detector. Prior to test, the sample was reduced by a H_2/Ar flow (10 vol.%, 100 mL/min) at 650 °C for 1 h and then flushed with an Ar stream (90 mL/min). Afterwards, the background of DRIFTS was obtained until the collected background spectra remained stable. Then, a CO_2/Ar stream (10 vol.%, 30 mL/min) was introduced to carry out CO_2 adsorption. After the CO_2 adsorption was saturated, the cell was flushed with an Ar stream. Then a CH_4/Ar (10 vol.%, 30 mL/min) stream was introduced for CH_4 adsorption.

2.4. DFT calculations

Spin polarized DFT + U calculations were carried out with the plane wave-based Vienna *ab initio* Simulation Package (VASP) [43]. The projector augmented wave (PAW) method which described the interactions between the atomic cores and electrons [44], along with the generalized-gradient approximation (GGA) in the form of the Perdew-Burke-Ernzerhof (PBE) exchange-correlation functional were employed in the calculation. An effective Hubbard U as 3 eV was used for La and the planewave basis set was chosen with a kinetic energy cutoff of 400 eV [45]. The Brillouin zone was sampled with Γ point.

La₂O₃ (001) was confirmed to be the exposed facet according to the lattice fringe as shown in Fig. 1e, which is consistent with a number of experimental studies as well as the theoretical work indicating that La₂O₃ (001) is the most stable facet of lanthanum oxide [46,47]. For bulk La₂O₃ in the hexagonal structure, the computed lattice constants were $a = b = 3.990 \text{ \AA}$, $c = 6.247 \text{ \AA}$, consistent with the experimental results $a = b = 3.939 \text{ \AA}$, $c = 6.136 \text{ \AA}$. The La₂O₃ (001) facet was represented with a 5×3 unit cell and separated by 15 Å of vacuum in the direction perpendicular to the slab surface, of which the dipole correction was included. The slab was four layers thick, which consisted of two repeated units along the c axis. Considering the relatively large Ni particle size (Table 1), a quasi-one-dimensional Ni nanowire that was

Table 1
Textural parameters of the samples.

Samples	Surface area (m ² /g) ^a	Average pore diameter (nm) ^a	Pore volume (cm ³ /g) ^a	Ni content (wt.%) ^b	Particle size of Ni (nm)	Ni surface area (m ² /g _{Ni}) ^c
La ₂ O ₃ -n	3.9	N/A	0.01	N/A	N/A	N/A
5Ni/La ₂ O ₃ -n	15.2/14.0	N/A/N/A	0.03/0.03	5.3	13.7 ^e /17.1 ^d	3.0/2.2
La ₂ O ₃ -m	211.5	5.1	0.35	N/A	N/A	N/A
5Ni/La ₂ O ₃ -m	172.1/125.7	5.2/6.0	0.30/0.25	5.5	4.6 ^e /5.5 ^c	16.3/11.2

^a Determined from nitrogen physisorption, reduced/spent catalysts.

^b Derived from ICP-OES.

^c Evaluated from XRD, reduced/spent catalysts.

^d Obtained from TEM images of spent catalysts.

^e Calculated from H₂ pulse chemisorption, reduced/spent catalysts.

three layers thick and two or three atoms wide supported on a planar La₂O₃ (001) substrate was applied. Such Ni nanowire was periodic along the shorter cell vector direction (Fig. S1). During geometry optimization, the top two layers of slab, together with the Ni nanowire and adsorbates were allowed to relax until the force on each atom is less than 0.02 eV/Å. The adsorption energy of CO₂ is defined as $E_{\text{ads}} = E_{\text{total}} - E_{\text{sub}} - E_{\text{CO}_2}$, where E_{total} is the total energy of the substrate with CO₂ adsorbed, while E_{sub} refers to the total energy of either clean La₂O₃ slab or Ni nanowire supported on La₂O₃ and E_{CO_2} represents the energy of CO₂ in the gas phase.

3. Results and discussion

3.1. Characterization of the fresh catalysts

Fig. S2a depicts the nitrogen physisorption isotherms of various samples. For La₂O₃-m support, the isotherm exhibited type IV behavior, with an obvious hysteresis loop in the relative pressure range of 0.6 to 0.8. A similar isotherm appeared in the case of the reduced 5Ni/La₂O₃-m catalyst. The pore size distributions (Fig. S2b) of mesoporous samples are all narrow and the main peaks are located in the range of 4–7 nm. In addition, Fig. S3 shows the low-angle XRD profiles of La₂O₃-m support and 5Ni/La₂O₃-m catalyst. It can be seen that two diffraction peaks appeared at $2\theta = 0.8^\circ$ and 1.4° , which correspond to the (100) and (110) planes in the *p6mm* 2D hexagonal ordered structure [31]. The characterization results confirm the ordered mesoporous structure of the samples. On the contrary, for the La₂O₃-n and 5Ni/La₂O₃-n samples, the isotherms exhibited type II behavior, which match well with those generally observed in non-porous materials. As shown in Table 1, the specific surface area of La₂O₃-m support (211.5 m²/g) is significantly larger than La₂O₃-n support (3.9 m²/g). In addition, 5Ni/La₂O₃-m maintained large specific surface area (172.1 m²/g) as well, especially considering the high calcination and reduction temperatures (650 °C), which indicates that the prepared La₂O₃-m material possesses excellent structural stability. TEM images of both supports are shown in Fig. S2c and Fig. S2d. In the case of La₂O₃-m support, the ordered mesostructure was observed compared to La₂O₃-n support. As shown in Fig. S2d, the cylindrical channels were distinctly observed in the circled area.

Fig. 1a presents the wide-angle XRD analysis of the samples, which is helpful to examine the nature of the Ni species and investigate the possible modifications of the La₂O₃ support. Diffraction lines related to La₂O₃ were observed for all the samples. It is obvious that the intensity of mesoporous samples is lower than the samples without mesopore structure, which is consistent with the difference in specific surface area. The formation of LaNiO₃ perovskite was detected in 5Ni/La₂O₃-n catalyst, which was formed by the reaction between support and Ni precursor during calcination. On the contrary, for calcined 5Ni/La₂O₃-m catalyst, no peaks associated with Ni species were detected, indicating the high dispersion of Ni species. After reduction, only the peaks of La₂O₃ and Ni appeared. The Ni particle size of 5Ni/La₂O₃-n catalyst (Table 1) was calculated from the Ni (111) facet peak in XRD patterns (Fig. S4) according to Scherrer's equation.

Fig. 1b exhibits H₂-TPR results of the two catalysts. There are obvious differences between the two catalysts, indicating that different degrees of metal-support interactions were formed during calcination. As reported in literature, 5Ni/La₂O₃-n exhibits three reduction peaks (I, II, III). The first hydrogen consumption (I) is evidenced at 300 °C, which corresponds to the reduction of Ni²⁺ species on the catalyst surface [48]. The second peak (II) appears at 344 °C, which corresponds to the reduction of Ni³⁺ species to Ni²⁺ species and the formation of La₂Ni₂O₅ [49]. The third peak (III) appears at 563 °C, which corresponds to the reduction of Ni²⁺ in La₂Ni₂O₅ to metallic Ni. The second and third reduction peaks are consistent with the reduction process of LaNiO₃ perovskite [49]. Two reduction peaks (IV, V) appeared on 5Ni/La₂O₃-m catalyst. The low temperature peak (IV) corresponds to the reduction of Ni species having weak interaction with the support [26,30], and the high temperature peak (V) is derived from the reduction of nickel species having strong interaction with the support [50,51]. It is noted that, for 5Ni/La₂O₃-n catalyst, certain amount of the Ni species were embedded in the La₂O₃ matrix and covered by La₂O₃, which cannot be reduced during the reduction process [26,30,52]. The reduction degree of 5Ni/La₂O₃-n catalyst is 68%, which is lower than that of 5Ni/La₂O₃-m catalyst (83%).

TEM images of reduced 5Ni/La₂O₃-m catalysts are shown in Fig. 1d. The 5Ni/La₂O₃-m catalyst maintained the mesostructure after calcination and reduction. It is obvious that Ni particles in the 5Ni/La₂O₃-m have smaller sizes compared to 5Ni/La₂O₃-n catalyst (Table 1), which agrees with the XRD analysis. Further, the particle distribution of Ni in 5Ni/La₂O₃-n catalyst (Fig. 1c) is uneven. There are large amount of unutilized areas and only a few scattered areas with segregated Ni particles. On the contrary, Ni dispersion and particle size distribution are uniform for 5Ni/La₂O₃-m catalyst. As shown in Fig. 1e, La₂O₃ mainly exposes (001) facet and there is interface formed between Ni and La₂O₃ [23].

3.2. DRM activity and stability test

Fig. 2 shows the results of the stability test, where no significant deactivation of 5Ni/La₂O₃-m and 5Ni/La₂O₃-n catalysts were observed. For both catalysts, on account of the reverse water gas shift reaction (RWGS, Reaction 2), the conversion of CO₂ is higher than that of CH₄ and the H₂/CO ratio is slightly lower than the stoichiometric ratio of one. It is noteworthy that there was an induction period for 5Ni/La₂O₃-n catalyst before its catalytic activity reached maximum. This is because the nickel elements covered by La₂O₃ were gradually reduced in the initial stage of the reaction [52,53]. Fig. S5 (a) (b) show the CH₄-TPSR profiles of the catalysts. The results of CH₄-TPSR suggest that more CH₄ was activated on 5Ni/La₂O₃-m catalyst. The initial temperature of CH₄ activation on 5Ni/La₂O₃-m catalyst (260 °C) was lower than that of 5Ni/La₂O₃-n catalyst (341 °C), which indicates that 5Ni/La₂O₃-m catalyst has better CH₄ activation performance on account of its better nickel dispersion, smaller nickel particle size and more exposed nickel active sites (Table 1). The performance of recently reported Ni-based DRM catalysts was summarized in Table S1. It can be seen that for the

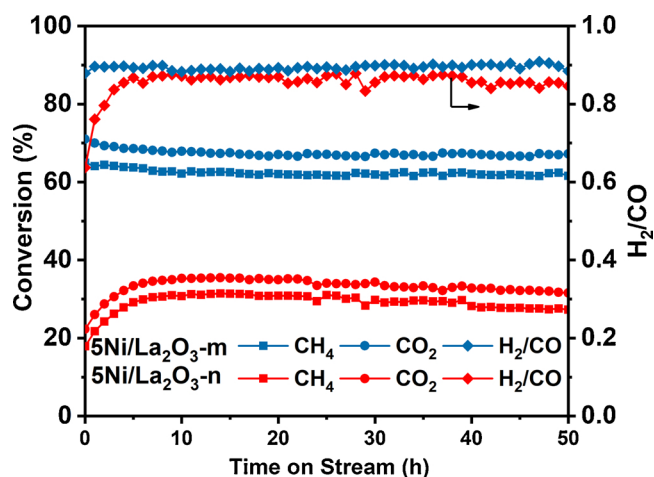


Fig. 2. Activity test of the catalysts. Reaction conditions: $\text{CH}_4/\text{CO}_2/\text{N}_2 = 15/15/70$, $\text{GHSV} = 240,000 \text{ mL} \cdot \text{h}^{-1} \cdot \text{g}_{\text{cat}}^{-1}$, 650°C , 1 atm.

catalyst of $\text{Ni}/\text{La}_2\text{O}_3$ system, $5\text{Ni}/\text{La}_2\text{O}_3\text{-m}$ catalyst has almost the same catalytic activity as LaNiO_3 although LaNiO_3 has a higher Ni content. In addition, $5\text{Ni}/\text{La}_2\text{O}_3\text{-m}$ catalyst exhibits excellent catalytic performance compared with other reported DRM catalysts.

3.3. Characterization of spent catalysts

Fig. S6 shows the nitrogen physisorption results of the spent catalysts. Both samples have similar nitrogen physisorption isotherms with corresponding supports and fresh catalysts, indicating that the $5\text{Ni}/\text{La}_2\text{O}_3\text{-m}$ catalyst has good structure stability. At the same time, the specific surface areas and pore volumes decreased after the 50 h stability test (Table 1). In view of the severe conditions during the DRM reaction, it is acceptable to have a slight sintering of La_2O_3 .

Fig. 3a exhibits the XRD patterns of spent catalysts. After the 50 h stability test, XRD analysis shows that the support of spent $5\text{Ni}/\text{La}_2\text{O}_3\text{-n}$ catalyst was transformed into $\text{La}_2\text{O}_2\text{CO}_3$, while the support of spent $5\text{Ni}/\text{La}_2\text{O}_3\text{-m}$ catalyst remained as La_2O_3 . This indicates that $\text{La}_2\text{O}_2\text{CO}_3$ accumulated in $5\text{Ni}/\text{La}_2\text{O}_3\text{-n}$ catalyst due to the poor dispersion of Ni. It should be underlined that the XRD diffraction peak of Ni (111) facet ($2\theta = 44.5^\circ$) is close to that of the hexagonal $\text{La}_2\text{O}_2\text{CO}_3$ (110) facet ($2\theta = 44.4^\circ$) and it is difficult to distinguish these two species. Based on the TEM images (Fig. 3c), the Ni particle size of $5\text{Ni}/\text{La}_2\text{O}_3\text{-n}$ catalyst increased from 13.7 nm to 17.1 nm (Table 1) after 50 h stability test. At the same time, for $5\text{Ni}/\text{La}_2\text{O}_3\text{-m}$ catalyst, it is important to notice that Ni particle size increased slightly from 4.6 to 5.5 nm after 50 h reaction. It is considered that the sintering of smaller particles is more easily to occur than larger particles. The results show that Ni particle sintering was significantly inhibited due to the confinement effect of the mesoporous structure in $5\text{Ni}/\text{La}_2\text{O}_3\text{-m}$ catalyst [27,54]. In addition, a characteristic peak at around $2\theta = 26^\circ$ appeared in the XRD pattern of the spent $5\text{Ni}/\text{La}_2\text{O}_3\text{-n}$ catalyst, which is attributed to the graphitic coke.

TGA was conducted to measure the amount of carbon deposition as shown in Fig. 3b. The mass reduction at $100\text{--}200^\circ\text{C}$ corresponds to the desorption of impurities on the catalysts. The mass increase at $270\text{--}380^\circ\text{C}$ is due to the oxidation of metallic nickel. It can be seen that the $5\text{Ni}/\text{La}_2\text{O}_3\text{-m}$ catalyst produced less amount of coke. The carbon formation rate per mols of methane converted was 1.1 and 4.0 mg/mol for $5\text{Ni}/\text{La}_2\text{O}_3\text{-m}$ and $5\text{Ni}/\text{La}_2\text{O}_3\text{-n}$ catalysts, respectively. This shows that $5\text{Ni}/\text{La}_2\text{O}_3\text{-m}$ catalyst has a stronger capability to inhibit carbon deposition, especially considering its higher catalyst activity. For the reference $5\text{Ni}/\text{La}_2\text{O}_3\text{-n}$ catalyst, in addition to the weight loss caused by coke removal at intermediate temperatures, the peak of $\text{La}_2\text{O}_2\text{CO}_3$ decomposition appeared above 650°C . As indicated by XRD and TEM results, the accumulation of $\text{La}_2\text{O}_2\text{CO}_3$ in $5\text{Ni}/\text{La}_2\text{O}_3\text{-n}$ catalyst is caused

by the poor dispersion of Ni.

TEM measurements were conducted to characterize the morphology of the spent catalysts. It's noticed that a large amount of filamentous coke is deposited on the spent $5\text{Ni}/\text{La}_2\text{O}_3\text{-n}$ catalyst surface as shown in Fig. 3c. Although there is a small amount of filamentous carbon in the spent $5\text{Ni}/\text{La}_2\text{O}_3\text{-m}$ catalyst periphery, the structure of the catalyst was well maintained as shown in Fig. 3d and Fig. S7. In general, there are two kinds of coke, including encapsulated and filamentous coke [55,56]. Encapsulated coke formed by Boudouard reaction (Reaction 3) leads to catalyst deactivation because it tends to cover the active sites of catalyst [57,58]. In contrast, filamentous coke produced by methane decomposition (Reaction 4) [59] does not suppress the DRM reaction. According to DTG and TEM analysis, for both catalysts, only filamentous coke was produced. Therefore, the absence of encapsulated coke is one of the key factors that both catalysts maintain good stability.

3.4. CO_2 activation

TGA shows that $5\text{Ni}/\text{La}_2\text{O}_3\text{-m}$ produced less amount of carbon deposits than $5\text{Ni}/\text{La}_2\text{O}_3\text{-n}$ (Fig. 3b). $5\text{Ni}/\text{La}_2\text{O}_3\text{-m}$ has better nickel dispersion and smaller Ni particle size, as shown in Fig. 1a and Table 1. Chen et al. pointed out that the small-sized Ni particles possess stronger ability to inhibit carbon deposition [58]. This makes it necessary to explore whether $5\text{Ni}/\text{La}_2\text{O}_3\text{-m}$ catalyst has a better capability to inhibit carbon deposition because of the smaller Ni particle size. Therefore, $5\text{Ni}/\text{Al}_2\text{O}_3$ catalyst with similar particle sizes ($4\text{--}6 \text{ nm}$) as $5\text{Ni}/\text{La}_2\text{O}_3\text{-m}$ was prepared, as shown in Fig. S8. In contrast to the $5\text{Ni}/\text{La}_2\text{O}_3\text{-m}$ catalyst, $5\text{Ni}/\text{Al}_2\text{O}_3$ catalyst produced a large amount of coke under the same DRM condition (Fig. S8b and Fig. S8d). Such distinct difference indicates that the CO_2 activation by La_2O_3 is the key to the inhibition of carbon deposition for $5\text{Ni}/\text{La}_2\text{O}_3\text{-m}$ catalyst. Therefore, it is necessary to study the adsorption and activation of carbon dioxide. Fig S5 (c) (d) exhibit the CO_2 -TPSR profiles of the catalysts. The results of CO_2 -TPSR suggest the initial temperature of CO_2 involved in eliminating carbon deposits on $5\text{Ni}/\text{La}_2\text{O}_3\text{-m}$ catalyst (398°C) was lower than that of $5\text{Ni}/\text{La}_2\text{O}_3\text{-n}$ catalyst (416°C), which indicates that CO_2 does have the ability to eliminate carbon deposits and $5\text{Ni}/\text{La}_2\text{O}_3\text{-m}$ catalyst has better performance of coke elimination.

In situ DRIFTS were obtained during CO_2 adsorption for the range of $1100\text{--}1800 \text{ cm}^{-1}$ corresponding to the formation of species in strong CO_2 chemisorption, as shown in Fig. 4a. The full DRIFTS were shown in Fig. S9. Bidentate carbonate has the strong band at 1565 cm^{-1} with the coexistence bands at 1270 and 1019 cm^{-1} [60,61]. Monodentate carbonate has the strong band at 1326 cm^{-1} [36,62] with the coexistence bands at 1416 and 1070 cm^{-1} . The properties of CO_2 adsorption are directly related to the chemical nature of the sample [32,34,63,64]. The formations of monodentate carbonate and bidentate carbonate correspond to isolated O^{2-} anions site and Lewis acid-base pairs ($\text{La}^{3+}\text{-O}^{2-}$ pair site), respectively [65,66]. For all the supports and catalysts, bidentate carbonate and monodentate carbonate coexist. Comparing to $\text{La}_2\text{O}_3\text{-n}$ support, although $\text{La}_2\text{O}_3\text{-m}$ has higher intensities of both carbonates, the intensity ratio between bidentate carbonate and monodentate carbonate (denoted as $I_{\text{B}}/I_{\text{M}}$) is similar (Table S2). After loading the active metal Ni, catalysts have higher $I_{\text{B}}/I_{\text{M}}$ compared to corresponding supports. In the mean time, $5\text{Ni}/\text{La}_2\text{O}_3\text{-m}$ has higher $I_{\text{B}}/I_{\text{M}}$ than $5\text{Ni}/\text{La}_2\text{O}_3\text{-n}$ (Table S2). These results indicate that the addition of Ni promotes the formation of bidentate carbonates on La_2O_3 and this promotion effect is more obvious on $5\text{Ni}/\text{La}_2\text{O}_3\text{-m}$ catalyst.

In situ DRIFTS measurements were performed to study the active intermediates formed during CO_2 adsorption. After carbonates formed on the catalysts were saturated during CO_2 adsorption and gas-phase CO_2 in the cell was flushed, CH_4 was introduced to react with carbonates on the catalyst surface. It's generally accepted that CH_4 dissociates to form coke precursor on Ni surface active sites, then coke precursor reacts with carbonate to form CO. Fig. 4b and Fig. S10 show the DRIFTS during CH_4 adsorption. For both catalysts, the intensity of

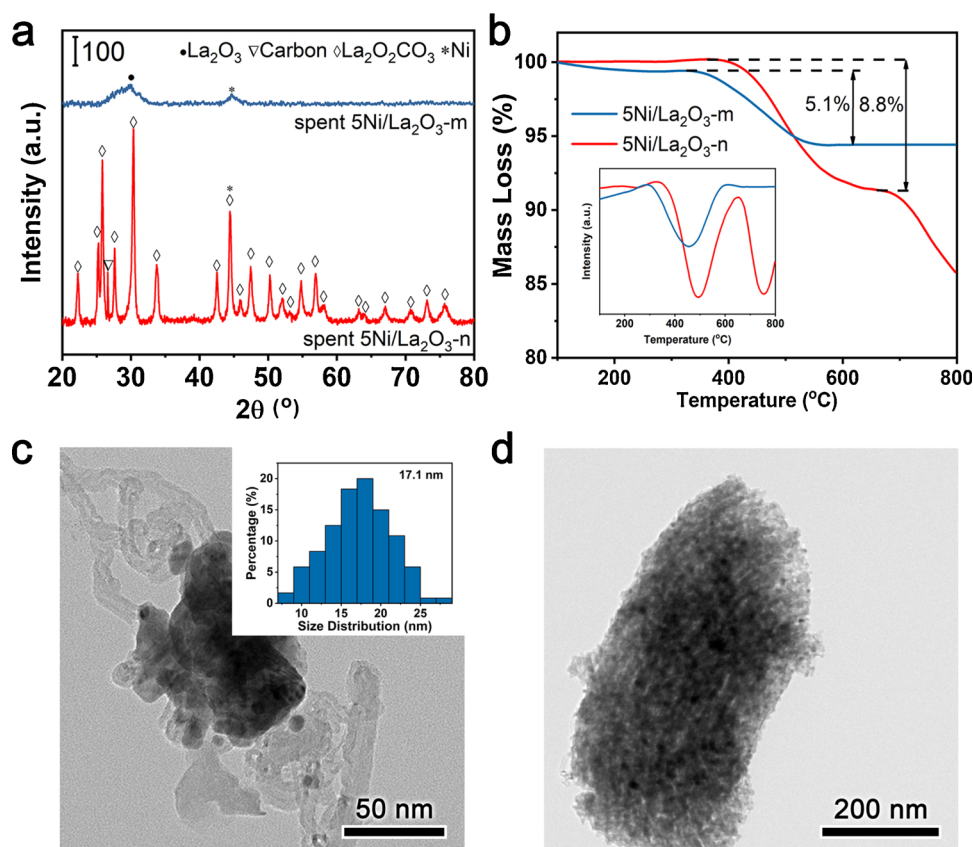


Fig. 3. Characterization of spent catalysts. **a** XRD patterns of spent catalysts. **b** TGA and DTG profiles (inset) for spent catalysts. **c** TEM image and Ni particle size distribution (inset) of spent 5Ni/La₂O₃-n catalyst. **d** TEM image of spent 5Ni/La₂O₃-m catalyst.

bidentate carbonate gradually decreased, while the intensity of monodentate carbonate kept almost constant, which suggests that bidentate carbonate can effectively react with the coke intermediate. In addition, CO₂/CH₄-TPSR was performed to obtain the *in situ* reaction information, as shown in Fig. S5 (e) (f). For both catalysts, methane activation and CO formation occurred simultaneously, indicating that CO₂ participates in the reaction pathway and reacts with carbon species to suppress carbon deposition. Many studies [23–25,28] have concluded

that the interface between Ni and La₂O₃ is active site for the reaction of coke precursor and CO₂-derived species. Combined with the above experimental results, it is reasonable to propose that the interface between Ni and La₂O₃ promotes the formation of bidentate carbonate, which participates in the process of coke removal. This will be further discussed by DFT calculations in the following section.

CO₂-TPD was employed to quantitatively evaluate the number of various basic sites on the samples. As exhibited in Fig. 5 and Table S3,

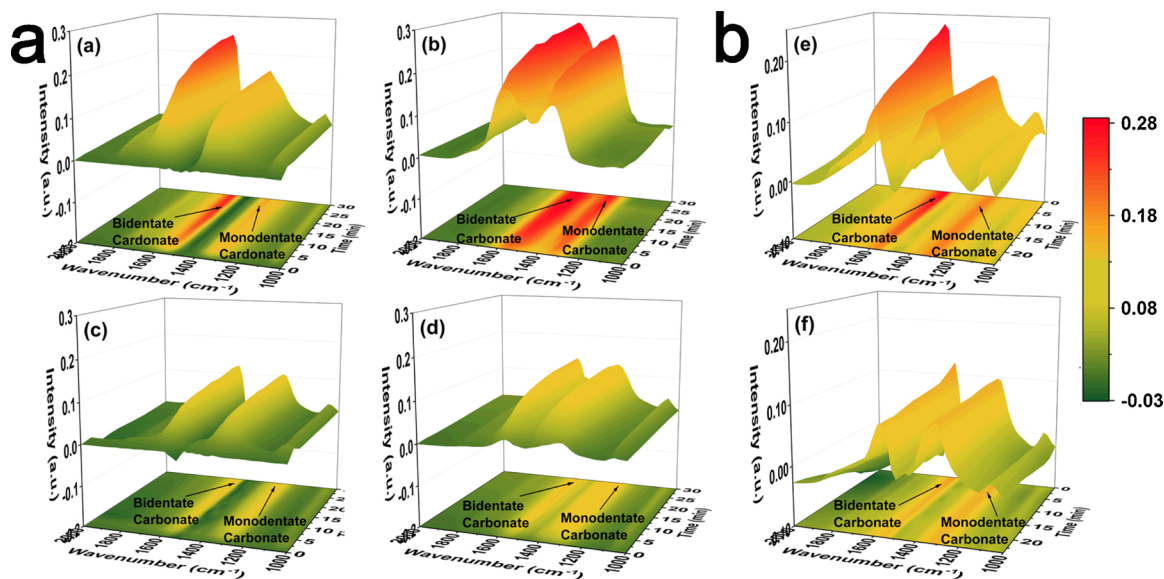


Fig. 4. *In situ* DRIFTS measurements. **a** DRIFTS for (a) 5Ni/La₂O₃-m, (b) La₂O₃-m, (c) 5Ni/La₂O₃-n and (d) La₂O₃-n during CO₂ adsorption. **b** DRIFTS for (e) 5Ni/La₂O₃-m and (f) 5Ni/La₂O₃-n during CH₄ adsorption.

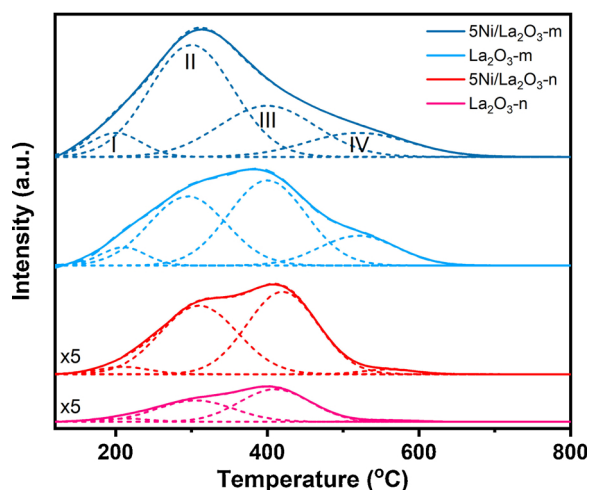


Fig. 5. CO₂-TPD results of the supports and catalysts.

four types of basic sites (named as I, II, III, IV) can be divided according to different CO₂ desorption temperature range [60,61,67]. Typically, the desorption peaks at 200, 300, and 400 °C correspond to three types of carbonate species [65,68]: bicarbonate (I), bidentate (II) and monodentate (III) carbonates, respectively. IV corresponds to the decomposition of surface La₂O₂CO₃ formed during CO₂ adsorption. Comparing to La₂O₃-n support, La₂O₃-m support has more CO₂ adsorption sites on account of its larger specific surface area. However, the ratio of bidentate carbonate/monodentate carbonate (denoted as N_B/N_M) (Table S2) is similar. In addition, catalysts have higher N_B/N_M comparing to corresponding supports, and 5Ni/La₂O₃-m has higher N_B/N_M than 5Ni/La₂O₃-n (Table S2). These results are consistent with *in situ* DRIFTS during CO₂ adsorption. Therefore, CO₂-TPD draws the same conclusion as *in situ* DRIFTS that the addition of Ni promotes the formation of bidentate carbonates on La₂O₃ and 5Ni/La₂O₃-m catalyst has stronger capability to facilitate the formation of bidentate carbonate.

The proposed CO₂ activation mechanism well corroborates with the characterization results of spent catalysts. For 5Ni/La₂O₃-m catalyst, CO₂-derived species can react timely with the carbon species generated from CH₄ activation on nickel. Therefore, no accumulation of La₂O₂CO₃

happened due to the better Ni dispersion of 5Ni/La₂O₃-m. Furthermore, many studies found that the most important factors affecting carbon deposition are Ni particle size [58,69,70] and support properties [71]. *In situ* DRIFTS and CO₂-TPD results have confirmed that both supports have similar chemical properties for CO₂ activation, and the addition of Ni promotes the formation of bidentate carbonate on La₂O₃. In addition, by comparing the 5Ni/Al₂O₃ and 5Ni/La₂O₃-m catalysts, it was proved that the small particle size Ni can not inhibit carbon deposition. Therefore, it is proposed that the difference in coke formation on 5Ni/La₂O₃-m and 5Ni/La₂O₃-n catalysts is mainly attributed to the different interface between Ni and La₂O₃, which will be discussed in the following section.

3.5. DFT calculations of CO₂ activation

DFT calculations were applied to demonstrate how the interface between Ni and La₂O₃ affects the CO₂ activation. The adsorption energies of CO₂ are calculated at the Ni (111) and La₂O₃ (001) interface or La₂O₃ (001) surface. Owing to the lattice mismatch, there is slight movement of Ni nanowire on La₂O₃(001) surface. To exclude such effect, different loading sites of Ni nanowire have been tested for comparison (Fig. S11). The absolute energies of two kinds of quasi-one-dimensional nanowire models are quite close, and Model b in Fig. S11b has a lower energy by 0.35 eV. With CO₂ adsorbed on the interface, Model a in Fig. S11a changes its geometric structure and performs like Fig. S11b. The adsorption energies of CO₂ on the interface of Fig. S11a and Fig. S11b by forming monodentate carbonate are -0.48 eV and -0.12 eV, respectively. The adsorption energy difference is almost the same as energy difference between the two models, which can be viewed as the influence of geometric structure transformation. Model Fig. S11b was applied for the following calculation.

Based on experimental results, DFT calculations focused on two activation modes of CO₂, *i.e.* bidentate and monodentate carbonate. In the case of La₂O₃ support, as shown in Fig. 6 and Table S4, DFT calculation results illustrate that the adsorption energies of CO₂ are quite similar to generate bidentate and monodentate carbonate (-1.05 eV and -0.94 eV, respectively), which is in accordance with the experimental results that the amounts of bidentate carbonate and monodentate carbonate are almost the same (Table S3). In the case of Ni/La₂O₃ catalyst, the adsorption energy of CO₂ to generate bidentate carbonate is -2.64 eV, which is ~2.5 eV lower than that to generate monodentate

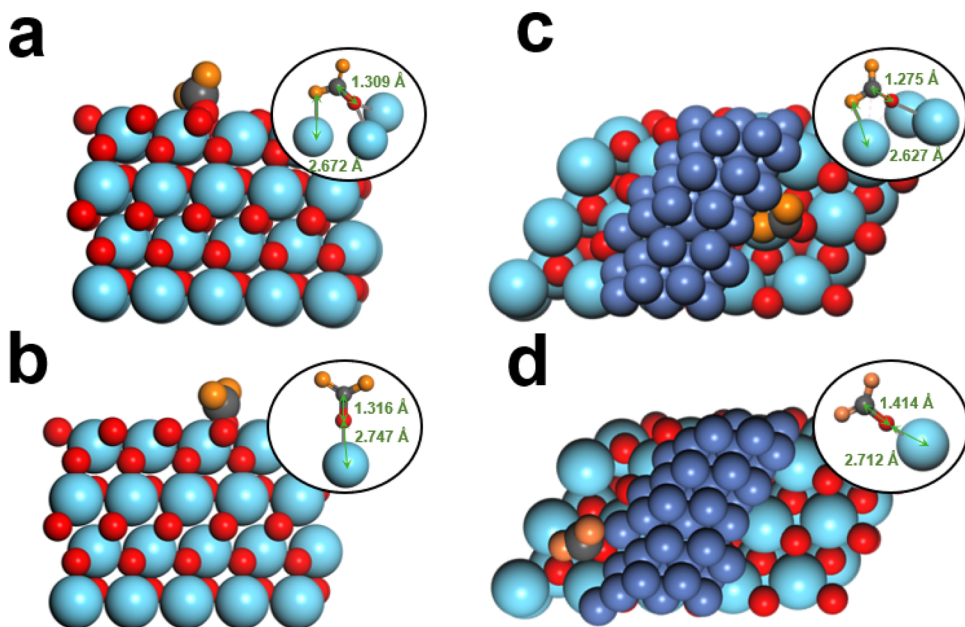


Fig. 6. DFT calculations of CO₂ activation. CO₂ adsorption on La₂O₃ and at the interface of Ni and La₂O₃ to form a, c bidentate carbonate and b, d monodentate carbonate. Colors: La - cyan; O - red & orange; C - gray; Ni - steelblue (For interpretation of the references to colour in this figure legend, the reader is referred to the web version of this article).



Scheme 1. Proposed Ni/La₂O₃ catalyst model in the DRM process.

carbonate (-0.12 eV). Such significant difference reveals that it tends to form bidentate carbonate instead of monodentate carbonate at the interface during CO₂ activation. In the experiment, it's observed that the introduction of Ni to La₂O₃ support promoted the formation of bidentate carbonate, and bidentate carbonate is proved to be active in the process of coke removal. At the same time, the interface between Ni and La₂O₃ is the active site for the reaction taking place. Therefore, we believe that the formation of bidentate carbonate is promoted at the interface between Ni and La₂O₃. In addition, because of the better Ni dispersion in the 5Ni/La₂O₃-m catalyst, more interfaces are formed, resulting in the formation of more bidentate carbonate.

According to the theoretical and experimental results, the catalyst model and possible reaction mechanism are proposed as shown in Scheme 1. CH₄ is activated on Ni particle surface forming activated coke precursors and H₂. CO₂ adsorption forms bidentate carbonate at the interface between Ni and La₂O₃. Bidentate carbonate reacts with adjacent activated coke precursors to form CO. Therefore, only Ni in close contact with the support at the interface can avoid carbon deposition [25,72]. For 5Ni/La₂O₃-m catalyst, more Ni/La₂O₃ interface exists because it has better nickel dispersion. As a result, the amount of coke deposited on the 5Ni/La₂O₃-m catalyst is significantly reduced.

4. Conclusions

We have prepared mesoporous La₂O₃ with large specific surface area (211.5 m²/g). In the case of the mesoporous Ni/La₂O₃ catalyst, the mesoporous architecture, large surface area and large pore volume could supply more catalytically active Ni sites accessible to the reactants, resulting in higher reforming activity. In addition, carbon deposition and Ni metal sintering were significantly suppressed on the mesoporous Ni/La₂O₃ catalyst due to the confinement of La₂O₃-m support. According to *in situ* DRIFTS, TPSR, CO₂-TPD and DFT calculations results, it is confirmed that the interface between Ni and La₂O₃ can promote the formation of bidentate carbonate. Bidentate carbonate was found active to react with coke intermediate derived from methane activation to inhibit carbon deposition. 5Ni/La₂O₃-m catalyst can promote the formation of more bidentate carbonate due to the increased interface by enhanced Ni dispersion. In addition, the better dispersion of coke precursors generated on Ni can more easily react with the bidentate carbonate at the interface between Ni and La₂O₃. Consequently, less carbon deposition was formed for the 5Ni/La₂O₃-m catalyst during the DRM reaction process. Our work illustrates the importance of the interface between Ni and La₂O₃ from the perspective of carbon dioxide activation for Ni/La₂O₃ catalyst, which will guide the design and synthesis of reforming catalysts with superior and stable performance.

Declaration of Competing Interest

The authors declare that they have no known competing financial interests or personal relationships that could have appeared to influence the work reported in this paper.

Acknowledgments

We thank the National Key R&D Program of China (2016YFB0600901), the National Natural Science Foundation of China (No. 51761145012, 21525626, U1663224) and the Program of Introducing Talents of Discipline to Universities (No. B06006) for financial support.

References

- [1] F. Polo-Garzon, D. Pakhare, J.J. Spivey, D.A. Bruce, Dry reforming of methane on Rh-Doped pyrochlore catalysts: a steady-state isotopic transient kinetic study, *ACS Catal.* 6 (2016) 3826–3833, <https://doi.org/10.1021/acscatal.6b00666>.
- [2] S. Kawi, Y. Kathiraser, J. Ni, U. Oemar, Z. Li, E.T. Saw, Progress in synthesis of highly active and stable nickel-based catalysts for carbon dioxide reforming of methane, *ChemSusChem* 8 (2015) 3556–3575, <https://doi.org/10.1002/cssc.201500390>.
- [3] N. Channuranasiri, A.M. Ribeiro, A.E. Rodrigues, A. Arpornwathanop, N. Laosiripojana, P. Praserttham, S. Assabumrungrat, Hydrogen production via sorption enhanced steam methane reforming process using Ni/CaO multifunctional catalyst, *Ind. Eng. Chem. Res.* 50 (2011) 13662–13671, <https://doi.org/10.1021/ie201226j>.
- [4] O.R. Inderwildi, S.J. Jenkins, D.A. King, Mechanistic studies of hydrocarbon combustion and synthesis on noble metals, *Angew. Chem. Int. Ed.* 47 (2008) 5253–5255, <https://doi.org/10.1002/anie.200800685>.
- [5] W. Chen, G. Zhao, Q. Xue, L. Chen, Y. Lu, High carbon-resistance Ni/CeAlO₃-Al₂O₃ catalyst for CH₄/CO₂ reforming, *Appl. Catal. B* 136–137 (2013) 260–268, <https://doi.org/10.1016/j.apcatb.2013.01.044>.
- [6] D. Li, X. Li, J. Gong, Catalytic reforming of oxygenates: state of the art and future prospects, *Chem. Rev.* 116 (2016) 11529–11653, <https://doi.org/10.1021/acs.chemrev.6b00099>.
- [7] D. Pakhare, J. Spivey, A review of dry (CO₂) reforming of methane over noble metal catalysts, *Chem. Soc. Rev.* 43 (2014) 7813–7837, <https://doi.org/10.1039/c3cs60395d>.
- [8] S. Li, J. Gong, Strategies for improving the performance and stability of Ni-based catalysts for reforming reactions, *Chem. Soc. Rev.* 43 (2014) 7245–7256, <https://doi.org/10.1039/c4cs00223g>.
- [9] D. Chen, L. He, Towards an efficient hydrogen production from biomass: a review of processes and materials, *ChemCatChem* 3 (2011) 490–511, <https://doi.org/10.1002/cctc.201000345>.
- [10] H. Tian, X. Li, L. Zeng, J. Gong, Recent advances on the design of group VIII base-metal catalysts with encapsulated structures, *ACS Catal.* 5 (2015) 4959–4977, <https://doi.org/10.1021/acscatal.5b01221>.
- [11] Y. Lou, M. Steib, Q. Zhang, K. Tiefenbacher, A. Horváth, A. Jentys, Y. Liu, J.A. Lercher, Design of stable Ni/ZrO₂ catalysts for dry reforming of methane, *J. Catal.* 356 (2017) 147–156, <https://doi.org/10.1016/j.jcat.2017.10.009>.
- [12] S.M. Stagg-Williams, F.B. Noronha, G. Fendley, D.E. Resasco, CO₂ Reforming of CH₄ over Pt/ZrO₂ Catalysts Promoted with La and Ce Oxides, *J. Catal.* 194 (2000) 240–249, <https://doi.org/10.1006/jcat.2000.2939>.

- [13] L. Foppa, M.-C. Silaghi, K. Larmier, A. Comas-Vives, Intrinsic reactivity of Ni, Pd and Pt surfaces in dry reforming and competitive reactions: insights from first principles calculations and microkinetic modeling simulations, *J. Catal.* 343 (2016) 196–207, <https://doi.org/10.1016/j.jcat.2016.02.030>.
- [14] W. Tu, M. Ghoussoub, C.V. Singh, Y.C. Chin, Consequences of surface oxophilicity of Ni, Ni-Co, and Co clusters on methane activation, *J. Am. Chem. Soc.* 139 (2017) 6928–6945, <https://doi.org/10.1021/jacs.7b01632>.
- [15] S.M. Kim, P.M. Abdala, T. Margossian, D. Hosseini, L. Foppa, A. Armutlulu, W. van Beek, A. Comas-Vives, C. Copéret, C. Müller, Cooperativity and dynamics increase the performance of NiFe dry reforming catalysts, *J. Am. Chem. Soc.* 139 (2017) 1937–1949, <https://doi.org/10.1021/jacs.6b11487>.
- [16] P. Kuai Pan, Y. Liu, Q. Ge, C.-j. Liu, Promotion effects of Ga₂O₃ on CO₂ adsorption and conversion over a SiO₂-supported Ni catalyst, *Energy Environ. Sci.* 3 (2010) 1322–1325, <https://doi.org/10.1021/c0ee00149j>.
- [17] L. Mo, K.K.M. Leong, S. Kawi, A highly dispersed and anti-coking Ni-La₂O₃/SiO₂ catalyst for syngas production from dry carbon dioxide reforming of methane, *Catal. Sci. Technol.* 4 (2014) 2107–2114, <https://doi.org/10.1039/c3cy00869j>.
- [18] C. Shi, P. Zhang, Effect of a second metal (Y, K, Ca, Mn or Cu) addition on the carbon dioxide reforming of methane over nanostructured palladium catalysts, *Appl. Catal. B* 115–116 (2012) 190–200, <https://doi.org/10.1016/j.apcatb.2011.12.002>.
- [19] J. Phromprasit, J. Powell, S. Wongsakulphasatch, W. Kiatkittipong, P. Bumroongsakulawat, S. Assabumrungrat, H₂ production from sorption enhanced steam reforming of biogas using multifunctional catalysts of Ni over Zr-, Ce- and La-modified CaO sorbents, *Chem. Eng. J.* 313 (2017) 1415–1425, <https://doi.org/10.1016/j.cej.2016.11.051>.
- [20] S.A. Theofanidis, V.V. Galvita, H. Poelman, G.B. Marin, Enhanced carbon-resistant dry reforming Fe-Ni catalyst: role of Fe, *ACS Catal.* 5 (2015) 3028–3039, <https://doi.org/10.1021/acscatal.5b00357>.
- [21] Y.-H. Wang, H.-M. Liu, B.-Q. Xu, Durable Ni/MgO catalysts for CO₂ reforming of methane: activity and metal-support interaction, *J. Mol. Catal. A Chem.* 299 (2009) 44–52, <https://doi.org/10.1016/j.molcata.2008.09.025>.
- [22] J.H. Bitter, K. Seshan, J.A. Lercher, Deactivation and coke accumulation during CO₂/CH₄ reforming over Pt catalysts, *J. Catal.* 183 (1999) 336–343 <https://doi.org/jcat.1999.2402>.
- [23] A. Slagtern, Y. Schuurman, C. Leclercq, X. Verykios, C. Mirodatos, Specific features concerning the mechanism of methane reforming by carbon dioxide over Ni/La₂O₃ catalyst, *J. Catal.* 172 (1997) 118–126, <https://doi.org/10.1006/jcat.1997.1823>.
- [24] O.V. Manoilova, S.G. Podkolzin, B. Tope, J. Lercher, E.E. Stangland, J.-M. Goupil, B.M. Weckhuysen, Surface Acidity and Basicity of La₂O₃, LaOCl, and LaCl₃ Characterized by IR Spectroscopy, TPD, and DFT Calculations, *J. Phys. Chem. B* 108 (2004) 15770–15781, <https://doi.org/10.1021/jp040311m>.
- [25] V.A. Tspouriari, X.E. Verykios, Kinetic study of the catalytic reforming of methane with carbon dioxide to synthesis gas over Ni/La₂O₃ catalyst, *Catal. Today* 64 (2001) 83–90, [https://doi.org/10.1016/S0920-5861\(00\)00511-3](https://doi.org/10.1016/S0920-5861(00)00511-3).
- [26] X. Li, D. Li, H. Tian, L. Zeng, Z.-J. Zhao, J. Gong, Dry reforming of methane over Ni/La₂O₃ nanorod catalysts with stabilized Ni nanoparticles, *Appl. Catal. B* 202 (2017) 683–694, <https://doi.org/10.1016/j.apcatb.2016.09.071>.
- [27] M.M. Nair, S. Kaliaguine, F. Kleitz, Nanocast LaNiO₃ perovskites as precursors for the preparation of coke-resistant dry reforming catalysts, *ACS Catal.* 4 (2014) 3837–3846, <https://doi.org/10.1021/cs500918c>.
- [28] V.A. Tspouriari, X.E. Verykios, Carbon and oxygen reaction pathways of CO₂ reforming of methane over Ni/La₂O₃ and Ni/Al₂O₃ catalysts studied by isotopic tracing techniques, *J. Catal.* 187 (1999) 85–94 <https://doi.org/jcat.1999.2565>.
- [29] Z. Boukha, L. Fitian, M. López-Haro, M. Mora, J.R. Ruiz, C. Jiménez-Sanchidrián, G. Blanco, J.J. Calvino, G.A. Cifredo, S. Bernal, Influence of the calcination temperature on the nano-structural properties, surface basicity, and catalytic behavior of alumina-supported lanthana samples, *J. Catal.* 272 (2010) 121–130, <https://doi.org/10.1016/j.jcat.2010.03.005>.
- [30] G. Garbarino, C. Wang, I. Valsamakis, S. Chitsazan, P. Riani, E. Finocchio, M. Flytzani-Stephanopoulos, G. Busca, A study of Ni/Al₂O₃ and Ni-La/Al₂O₃ catalysts for the steam reforming of ethanol and phenol, *Appl. Catal. B* 174–175 (2015) 21–34, <https://doi.org/10.1016/j.apcatb.2015.02.024>.
- [31] H. Ma, L. Zeng, H. Tian, D. Li, X. Wang, X. Li, J. Gong, Efficient hydrogen production from ethanol steam reforming over La-modified ordered mesoporous Ni-based catalysts, *Appl. Catal. B* 181 (2016) 321–331, <https://doi.org/10.1016/j.apcatb.2015.08.019>.
- [32] D. Pakhare, V. Schwartz, V. Abdelsayed, D. Haynes, D. Shekhawat, J. Poston, J. Spivey, Kinetic and mechanistic study of dry (CO₂) reforming of methane over Rh-substituted La₂Zr₂O₇ pyrochlores, *J. Catal.* 316 (2014) 78–92, <https://doi.org/10.1016/j.jcat.2014.04.023>.
- [33] H. Wang, X. Dong, T. Zhao, H. Yu, M. Li, Dry reforming of methane over bimetallic Ni-Co catalyst prepared from La(Co_{0.5}Ni_{1.5})_{0.5}Fe_{0.5}O₃ perovskite precursor: catalytic activity and coking resistance, *Appl. Catal. B* 245 (2019) 302–313, <https://doi.org/10.1016/j.apcatb.2018.12.072>.
- [34] A. Tsoukalou, Q. Imtiaz, S.M. Kim, P.M. Abdala, S. Yoon, C.R. Müller, Dry-reforming of methane over bimetallic Ni-M/La₂O₃ (M = Co, Fe): the effect of the rate of La₂O₃/CO₂ formation and phase stability on the catalytic activity and stability, *J. Catal.* 343 (2016) 208–214, <https://doi.org/10.1016/j.jcat.2016.03.018>.
- [35] S. Iruata, L.M. Cornaglia, E.A. Lombardo, Effects of rhodium and platinum on the reactivity of lanthanum phases, *Mater. Chem. Phys.* 86 (2004) 440–447, <https://doi.org/10.1016/j.matchemphys.2004.04.017>.
- [36] J.F. Múnera, S. Iruata, L. Cornaglia, E.A. Lombardo, D.V. Cesar, M. Schmal, Kinetics and reaction pathway of the CO₂ reforming of methane on Rh supported on lanthanum-based solid, *J. Catal.* 245 (2007) 25–34, <https://doi.org/10.1016/j.jcat.2006.09.008>.
- [37] X. Li, Z.-J. Zhao, L. Zeng, J. Zhao, H. Tian, S. Chen, K. Li, S. Sang, J. Gong, On the role of Ce in CO₂ adsorption and activation over lanthanum species, *Chem. Sci.* 9 (2018) 3426–3437, <https://doi.org/10.1039/c8sc00203g>.
- [38] Z. Zhang, X.E. Verykios, S.M. MacDonald, S. Affrossman, Comparative study of carbon dioxide reforming of methane to synthesis gas over Ni/La₂O₃ and conventional nickel-based catalysts, *J. Phys. Chem.* 100 (1996) 744–754, <https://doi.org/10.1021/jp951809e>.
- [39] R.C. Rabelo-Neto, H.B.E. Sales, C.V.M. Inocêncio, E. Varga, A. Oszko, A. Erdohelyi, F.B. Noronha, L.V. Mattos, CO₂ reforming of methane over supported LaNiO₃ perovskite-type oxides, *Appl. Catal. B* 221 (2018) 349–361, <https://doi.org/10.1016/j.apcatb.2017.09.022>.
- [40] I.V. Yentekakis, G. Goula, M. Hatzisymeon, I. Betsi-Argyropoulou, G. Botzoulaki, K. Kousi, D.I. Kondarides, M.J. Taylor, C.M.A. Parlett, A. Osatiashtiani, G. Kyriakou, J.P. Holgado, R.M. Lambert, Effect of support oxygen storage capacity on the catalytic performance of Rh nanoparticles for CO₂ reforming of methane, *Appl. Catal. B* 243 (2019) 490–501, <https://doi.org/10.1016/j.apcatb.2018.10.048>.
- [41] D. Gu, W. Schmidt, C.M. Pichler, H.J. Bongard, B. Spliethoff, S. Asahina, Z. Cao, O. Terasaki, F. Schüth, Surface-Casting Synthesis of Mesoporous Zirconia with a CMK-5-Like Structure and High Surface Area, *Angew. Chem. Int. Ed.* 56 (2017) 1–5, <https://doi.org/10.1002/anie.201705042>.
- [42] C.H. Bartholomew, R.B. Pannell, The stoichiometry of hydrogen and carbon monoxide chemisorption on alumina- and silica-supported nickel, *J. Catal.* 65 (1980) 390–401, [https://doi.org/10.1016/0021-9517\(80\)90316-4](https://doi.org/10.1016/0021-9517(80)90316-4).
- [43] G. Kresse, J. Furthmüller, Efficiency of ab-initio total energy calculations for metals and semiconductors using a plane-wave basis set, *Comp. Mater. Sci.* 6 (1996) 15–50, [https://doi.org/10.1016/0927-0256\(96\)00008-0](https://doi.org/10.1016/0927-0256(96)00008-0).
- [44] G. Kresse, D. Joubert, From ultrasoft pseudopotentials to the projector augmented-wave method, *Phys. Rev. B: Condens. Matter Mater. Phys.* 59 (1999) 1758–1775, <https://doi.org/10.1103/PhysRevB.59.1758>.
- [45] V. Stevanović, S. Lany, X. Zhang, A. Zunger, Correcting density functional theory for accurate predictions of compound enthalpies of formation: fitted elemental-phase reference energies, *Phys. Rev. B: Condens. Matter Mater. Phys.* 85 (2012) 115104, <https://doi.org/10.1103/PhysRevB.85.115104>.
- [46] M.S. Palmer, M. Neurock, M.M. Olken, Periodic Density Functional Theory Study of Methane Activation over La₂O₃: Activity of O²⁻, O₂²⁻, Oxygen Point Defect, and Sr²⁺-Doped Surface Sites, *J. Am. Chem. Soc.* 124 (2002) 8452–8461, <https://doi.org/10.1021/ja0121235>.
- [47] S. Wang, L. Cong, C. Zhao, Y. Li, Y. Pang, Y. Zhao, S. Li, Y. Sun, First principles studies of CO₂ and O₂ chemisorption on La₂O₃ surfaces, *Phys. Chem. Chem. Phys.* 19 (2017) 26799–26811, <https://doi.org/10.1039/c7cp05471h>.
- [48] X. Xu, L. Li, F. Yu, H. Peng, X. Fang, X. Wang, Mesoporous high surface area NiO synthesized with soft templates: remarkable for catalytic CH₄ deep oxidation, *Mol. Catal.* 441 (2017) 81–91, <https://doi.org/10.1016/j.mcat.2017.08.005>.
- [49] G. Valderrama, A. Kiennemann, M.R. Goldwasser, Dry reforming of CH₄ over solid solutions of LaNi_{1-x}Co_xO₃, *Catal. Today* 133–135 (2008) 142–148, <https://doi.org/10.1016/j.cattod.2007.12.069>.
- [50] S. Li, M. Li, C. Zhang, S. Wang, X. Ma, J. Gong, Steam reforming of ethanol over Ni/ZrO₂ catalysts: effect of support on product distribution, *Int. J. Hydrogen Energy* 37 (2012) 2940–2949, <https://doi.org/10.1016/j.ijhydene.2011.01.009>.
- [51] S. Das, J. Ashok, Z. Bian, N. Dewangan, M.H. Wai, Y. Du, A. Borgna, K. Hidajat, S. Kawi, Silica-Ceria sandwiched Ni core-shell catalyst for low temperature dry reforming of biogas: coke resistance and mechanistic insights, *Appl. Catal. B* 230 (2018) 220–236, <https://doi.org/10.1016/j.apcatb.2018.02.041>.
- [52] S. Singh, D. Zubenko, B.A. Rosen, Influence of LaNiO₃ shape on its solid-phase crystallization into coke-free reforming catalysts, *ACS Catal.* 6 (2016) 4199–4205, <https://doi.org/10.1021/acscatal.6b00673>.
- [53] H. Chen, H. Yu, F. Peng, H. Wang, J. Yang, M. Pan, Efficient and stable oxidative steam reforming of ethanol for hydrogen production: effect of in situ dispersion of Ir over Ir/La₂O₃, *J. Catal.* 269 (2010) 281–290, <https://doi.org/10.1016/j.jcat.2009.11.010>.
- [54] D. Li, L. Zeng, X. Li, X. Wang, H. Ma, S. Assabumrungrat, J. Gong, Ceria-promoted Ni/SBA-15 catalysts for ethanol steam reforming with enhanced activity and resistance to deactivation, *Appl. Catal. B* 176–177 (2015) 532–541, <https://doi.org/10.1016/j.apcatb.2015.04.020>.
- [55] A. Gili, L. Schlicker, M.F. Bekheet, O. Görke, S. Penner, M. Grünbacher, T. Götsch, P. Littlewood, T.J. Marks, P.C. Stair, R. Schomäcker, A. Doran, S. Selve, U. Simon, A. Gurlo, Surface carbon as a reactive intermediate in dry reforming of methane to syngas on a 5% Ni/MnO catalyst, *ACS Catal.* 8 (2018) 8739–8750, <https://doi.org/10.1021/acscatal.8b01820>.
- [56] Z. Wang, X.M. Cao, J. Zhu, P. Hu, Activity and coke formation of nickel and nickel carbide in dry reforming: a deactivation scheme from density functional theory, *J. Catal.* 311 (2014) 469–480, <https://doi.org/10.1016/j.jcat.2013.12.015>.
- [57] Z. Shang, S. Li, L. Li, G. Liu, X. Liang, Highly active and stable alumina supported nickel nanoparticle catalysts for dry reforming of methane, *Appl. Catal. B* 201 (2017) 302–309, <https://doi.org/10.1016/j.apcatb.2016.08.019>.
- [58] D. Chen, K. Christensen, E. Ochoá-Fernandez, Z. Yu, B. Tøtdal, N. Latorre, A. Monzón, A. Holmen, Synthesis of carbon nanofibers: effects of Ni crystal size during methane decomposition, *J. Catal.* 229 (2005) 82–96, <https://doi.org/10.1016/j.jcat.2004.10.017>.
- [59] M. Németh, D. Srankó, J. Károlyi, F. Somodi, Z. Schay, G. Sáfrán, I. Sajó, A. Horváth, Na-promoted Ni/ZrO₂ dry reforming catalyst with high efficiency: details of Na₂O–ZrO₂–Ni interaction controlling activity and coke formation, *Catal. Sci. Technol.* 7 (2017) 5386–5401, <https://doi.org/10.1039/c7cy01011g>.
- [60] B. Klingenberg, M.A. Vannice, Influence of pretreatment on lanthanum nitrate, carbonate, and oxide powders, *Chem. Mater.* 8 (1996) 2755–2768, <https://doi.org/10.1021/cm9602555>.

- [61] S.C. Shen, X. Chen, S. Kawi, CO₂ adsorption over Si-MCM-41 materials having basic sites created by postmodification with La₂O₃, *Langmuir* 20 (2004) 9130–9137, <https://doi.org/10.1021/la049947v>.
- [62] J. Shen, R.D. Cortright, Y. Chen, J.A. Dumesic, Microcalorimetric and infrared spectroscopic studies of γ -Al₂O₃ modified by basic metal oxides, *J. Phys. Chem.* 98 (1994) 8067–8073, <https://doi.org/10.1021/j100084a025>.
- [63] X. Huang, C. Dang, H. Yu, H. Wang, F. Peng, Morphology Effect of Ir/La₂O₂CO₃ Nanorods with Selectively Exposed {110} Facets in Catalytic Steam Reforming of Glycerol, *ACS Catal.* 5 (2015) 1155–1163, <https://doi.org/10.1021/cs5014305>.
- [64] J. Ni, L. Chen, J. Lin, M.K. Schreyer, Z. Wang, S. Kawi, High performance of Mg-La mixed oxides supported Ni catalysts for dry reforming of methane: the effect of crystal structure, *Int. J. Hydrogen Energy* 38 (2013) 13631–13642, <https://doi.org/10.1016/j.ijhydene.2013.08.041>.
- [65] R. Shi, F. Wang, Y. Tana, X. Li, W. Huang, Shen, A highly efficient Cu/La₂O₃ catalyst for transfer dehydrogenation of primary aliphatic alcohols, *Green Chem.* 12 (2010) 108–113, <https://doi.org/10.1039/b919807p>.
- [66] S. Sato, R. Takahashi, M. Kobune, H. Gotoh, Basic properties of rare earth oxides, *Appl. Catal. A Gen.* 356 (2009) 57–63, <https://doi.org/10.1016/j.apcata.2008.12.019>.
- [67] J.I. Di Cosimo, C.R. Apesteguía, M.J.L. Ginés, E. Iglesia, Structural Requirements and Reaction Pathways in Condensation Reactions of Alcohols on Mg₃AlO₈ Catalysts, *J. Catal.* 190 (2000) 261–275, <https://doi.org/10.1006/jcat.1999.2734>.
- [68] J.I. Di Cosimo, V.K. Díez, M. Xu, E. Iglesia, C.R. Apesteguía, Structure and surface and catalytic properties of Mg-Al basic oxides, *J. Catal.* 178 (1998) 499–510, <https://doi.org/10.1006/jcat.1998.2161>.
- [69] D. Baudouin, U. Rodemerck, F. Krumeich, Ad. Mallmann, K.C. Szeto, H. Ménard, L. Veyre, J.-P. Candy, P.B. Webb, C. Thieuleux, C. Copéret, Particle size effect in the low temperature reforming of methane by carbon dioxide on silica-supported Ni nanoparticles, *J. Catal.* 297 (2013) 27–34, <https://doi.org/10.1016/j.jcat.2012.09.011>.
- [70] J.W. Han, J.S. Park, M.S. Choi, H. Lee, Uncoupling the size and support effects of Ni catalysts for dry reforming of methane, *Appl. Catal. B* 203 (2017) 625–632, <https://doi.org/10.1016/j.apcatb.2016.10.069>.
- [71] S.-H. Seok, S.H. Choi, E.D. Park, S.H. Han, J.S. Lee, Mn-promoted Ni/Al₂O₃ catalysts for stable carbon dioxide reforming of methane, *J. Catal.* 209 (2002) 6–15, <https://doi.org/10.1006/jcat.2002.3627>.
- [72] G.S. Gallego, C. Batiot-Dupeyrat, J. Barrault, F. Mondragón, Dual active-site mechanism for dry methane reforming over Ni/La₂O₃ produced from LaNiO₃ perovskite, *Ind. Eng. Chem. Res.* 47 (2008) 9272–9278, <https://doi.org/10.1021/ie800281t>.